Catalysis Today 251 (2015) 53–59

Contents lists available at ScienceDirect

Catalysis Today

journal homepage: www.elsevier.com/locate/cattod

FeSBA-15-supported ruthenium catalyst for the selective hydrogenolysis of carboxylic acids to alcoholic chemicals

Wenjing Li, Linmin Ye*, Jin Chen, Xinping Duan, Haiqiang Lin, Youzhu Yuan*

State Key Laboratory of Physical Chemistry of Solid Surfaces and National Engineering Laboratory for Green Chemical Productions of Alcohols-Ethers-Esters, College of Chemistry and Chemical Engineering, Xiamen University, Xiamen 361005, China

ARTICLE INFO

Article history:
Received 26 July 2014
Received in revised form 5 October 2014
Accepted 17 October 2014
Available online 3 December 2014

Keywords:
FeSBA-15
Acetic acid
Hydrogenolysis
Alcoholic chemicals
Ru–Fe bimetallic catalyst

ABSTRACT

Ordered mesoporous FeSBA-15-supported Ru catalysts are characterized by N_2 adsorption–desorption isotherm, H_2-temperature-programmed reduction, X-ray fluorescence, X-ray diffraction, X-ray photoelectron spectroscopy, and transmission electron microscopy analyses. Results suggest the co-existence of Fe oxide species highly dispersed in the frameworks of SBA-15 and Ru–Fe bimetallic nanoparticles. The concentration of Fe species is low and in the form of Ru–Fe alloys located on the catalyst surfaces following reduction pretreatment in 5% H_2–95% N_2 flow at 623 K for 4 h. The as-reduced Ru/FeSBA-15 catalysts efficiently and selectively hydrogenolyze short-chain carboxylic acids (e.g., acetic acid, propionic acid, butyric acid, levulinic acid, and lactic acid) to their corresponding alcoholic chemicals. Results indicate that 2% Ru/FeSBA-15 catalyst with 1.07% Fe content yields the highest performance and excellent stability, yielding 92.5% conversion of acetic acid and 85.2% selectivity to ethanol under optimized conditions. The improved catalytic performance of the FeSBA-15-supported Ru catalyst is mainly attributed to the coherent interactions between Fe and Ru species, as well as to the high dispersion of Fe oxides in the SBA-15 framework.

1. Introduction

The large-scale, efficient utilization of renewable biomass resources has become a demand for social and industrial development to produce chemicals and fuels. Most of biomass conversion technologies focus on alcohols, primarily ethanol (EtOH), which is the cleanest liquid fuel alternative to fossil fuels [1,2]. Alcohols can further be converted to alkanes with less energy losses. Carboxylate platforms can be efficiently used to produce biofuels and biochemicals from biomasses [3]. The fermentation of glucose to acetic acid (AcOH) followed by the hydrogenolysis of AcOH to EtOH prevents the emission of CO_2 (Reaction (1)) and achieves a 100% carbon yield [4].

$$C_6H_{12}O_6 \rightarrow 3CH_3COOH \rightarrow 3CH_3CH_2OH + 3H_2O \quad (1)$$

The carbon atoms of carboxylic group exhibit relatively high oxidation states. The removal of oxygen atoms by catalytic hydrogenation produces alcohol from biomass-derived feedstock [5]. This reaction synthesizes fatty alcohols from their corresponding carboxylic acids and esters [6]. Fatty alcohols are nonionic surfactants that are widely used in lubricants, resins, perfumes, cosmetics, shampoos, and conditioners [7]. These alcohols have been explored for potential uses in medicine, health supplements, and biofuels [8]. Low-cost, high-efficiency hydrogenolysis routes have been developed to open economically viable pathways from renewable resource-derived materials as alternatives to fossil-based chemicals. AcOH can be used to probe the absorption of carboxylic acid and the corresponding conversion kinetics because of its molecular simplicity and wide range of commercial applications.

Ni et al. reported a biocatalytic method to convert a broad range of carboxylic acids to corresponding primary alcohols with 100% selectivity in the presence of hydrogen at a lower temperature of 313 K [9]. However, the hydrogenolysis of short-chain carboxylic acids to alcohol in a vapor-phase, continuous flow system under mild conditions remains a problem. C—C bonds and alcohols can be hydrogenolyzed and excessively hydrogenated, which result in cracked products and alkanes, respectively [10–12]. The breakage of C—O bond, hydrogenation of C=O bond, and suppression of the C—C bond cleavages in carboxylic acids yield high selectivity toward the corresponding alcohols. Noble metals (e.g., Pt and Ru-based catalysts) have been intensively explored to hydrogenolyze carboxylic acids [8,10–18]. The effects of a second metal on the catalysts have been investigated to improve the activity and selectivity of noble

* Corresponding authors.
E-mail addresses: lmye@xmu.edu.cn (L. Ye), yzyuan@xmu.edu.cn (Y. Yuan).

http://dx.doi.org/10.1016/j.cattod.2014.10.044
0920-5861/

catalysts. For example, Jiang et al. reported that the introduction of Cu to Ru-based catalysts respectively improved and suppressed the C—O and C—C cleavages [19]. Miyake et al. revealed that the addition of appropriate amounts of Sn to Ru-based catalysts promoted catalytic activity and selectivity during the hydrogenation of fatty acid methyl esters to alcohols [20]. Toba et al. reported that Ru–Sn/Al_2O_3 catalysts demonstrated good yields in the hydrogenolysis of saturated carboxylic acids to their corresponding alcohols; however, the reported technique required high pressure and temperature [21].

SBA-15-supported Ru–Fe catalysts exhibited significant improvements in the catalytic performance for the hydrogenolysis of AcOH to EtOH compared with the monometallic counterparts and those that use SiO_2 as the carrier [17]. The Ru–Fe catalysts could also actively convert carboxylic acids (e.g., propionic acid, butyric acid, levulinic acid, and lactic acid) to their corresponding alcoholic chemicals. Characterization results indicated that a small portion of Fe species was alloyed with Ru, whereas FeO_{1+x} ($0 < x < 0.5$) was dispersed on the catalyst surfaces. As a matter of fact, iron-containing zeolites and mesoporous materials with high specific area, uniform pore size distribution, and large pore size can potentially support Ru catalysts. Therefore, in this study, FeSBA-15-supported Ru catalysts were prepared; the structural and catalytic properties of these catalysts were analyzed in connection to the hydrogenolysis of carboxylic acids.

2. Experimental

2.1. Catalyst preparation

AcOH, propionic acid, butyric acid, levulinic acid, lactic acid, 1,4-dioxane, EtOH, $RuCl_3 \cdot nH_2O$, and $Fe(NO_3)_3 \cdot H_2O$ were purchased from China Pharmaceutical Group Shanghai Chemical Reagent Co., Ltd. (Shanghai, China). Amphiphilic triblock copolymer $(EO)_{20}(PO)_{70}(EO)_{20}$ and tetraethyl orthosilicate were purchased from Sigma–Aldrich. Hydrogen and nitrogen were purchased from Linde Industrial Gases. All the reagents were used as received without further purification.

Ordered hexagonal mesoporous FeSBA-15 and SBA-15 were synthesized as previously described [22,23]. FeSBA-15 support was successfully synthesized with different Fe contents. FeSBA-15-supported Ru catalysts were impregnately prepared by incorporating a specific amount of $RuCl_3 \cdot nH_2O$ and 1.0 g FeSBA-15 with different Fe contents in acetone solution. After stirring for about 6 h, the mixture was evaporated, dried and calcined at 573 K for 4 h; this mixture was labeled as *x*% Ru/*y*% FeSBA-15. For comparative purposes, a Ru–Fe/SBA-15 catalyst was synthesized by co-impregnation and labeled as *x*% Ru–*y*% Fe/SBA-15-IM, where *x* and *y* represent the weight percentages.

2.2. Catalytic test

The hydrogenolysis of AcOH, propionic acid, butyric acid, and levulinic acid (10 wt% levulinic acid/1,4-dioxane solution) was performed in a fixed-bed reactor equipped with a computer-controlled auto-sampling system. A 0.20 g catalyst was placed into a glass tube and pretreated in 5% H_2–95% N_2 flow at 623 K for 4 h. The temperature of pure H_2 was reduced to the required reaction temperature. This gas was then fed into the reactor, and the pressure of the reaction system was controlled. The carboxylic acids were pumped into the reactor via a Series III digital high-performance liquid chromatography (HPLC) pump (Scientific Systems, Inc.). The oxygenates and gas-phase products (e.g., CH_4, CO_2, CO, and C_2H_6) were respectively detected using a gas chromatograph (GC) equipped with a flame ionization detector and KB-Wax capillary column (30 m × 0.32 mm × 0.33 μm), as well as another GC equipped with a thermal conductivity detector, Gaskuropack 54 column (length, 3 m), and active carbon column (length, 2 m). The calibrated area was normalized to calculate the conversion and product selectivities.

Lactic acid was hydrogenolyzed in a 50 mL steel autoclave with a magnetic stirrer. Subsequently, 10 mL 5% lactic acid aqueous solution and 0.10 g as-reduced catalyst were placed in the autoclave. The reactor was then purged thrice with 1.0 MPa H_2 (99.995%) and then pressurized to 3.0 MPa; the temperature was increased to 473 K. After the reaction, the solution was separated from the catalysts by decantation and analyzed by a HPLC (Shimadzu LC-20) equipped with a refractive index and UV–Vis detectors. The conversion and selectivity were calculated by normalizing the calibrated area.

2.3. Catalyst characterizations

Ru and Fe contents on the catalysts were determined by a S8-TIGER X-ray fluorescence spectrometer (XRF). The samples were prepared by mixing 0.20 g catalyst and 0.80 g boric acid and compressing into tablets (diameter, 36 mm; thickness, 2 mm).

Fe leaching was determined by inductively coupled plasma atomic emission spectrometry (ICP-AES) on a Thermo Elemental IRIS Intrepid II XSP. The liquid was evaporated to remove the organic compounds, and was then treated by aqua regia at 353 K for 30 min. The resultant solution was heated up to 363 K to evaporate the solvent. The residue was diluted with 5% HCl and filtrated to a 25 mL volumetric flask before measurement.

UV–Vis light diffuse reflectance spectroscopy (UV–Vis DRS) was performed on a Cary 5000 UV–Vis–NIR spectrophotometer (wavelength, 200–800 nm).

N_2 adsorption–desorption isotherms were obtained on a Micromeritics TriStar II 3020 porosimetry analyzer at 77.3 K. The specific surface area or the average pore diameter and pore size distribution were calculated based on the Brunauer–Emmett–Teller or Barrett–Joyner–Halenda method.

H_2-temperature-programmed reduction (H_2-TPR) profiles were measured in a Micromeritics AutoChem II 2920 Chemisorption Analyzer. H_2 consumption was detected by recording mass spectrometer signals ($m/e = 2$).

X-ray diffraction (XRD) patterns were obtained on a Philips PANalytical X'pert PRO diffractometer and Cu Kα radiation (operating voltage, 40 kV; current, 30 mA).

Transmission electron microscopy (TEM) images were generated using a Tecnai F30 electron microscope at an acceleration voltage of 300 V. The powder for TEM analysis was dispersed in EtOH and deposited into copper grids.

Metal dispersion was calculated according to CO chemisorption, which was performed using a Micromeritics ASAP 2020M+C. The sample was purged with high-purity H_2 (purity, 99.999%) at 623 K for 30 min and then evacuated for 30 min. CO was introduced after vacuum cooling to 308 K. The first isotherm (total CO uptake) was measured. The amount of chemisorbed CO was taken as the difference between the total and reversibly adsorbed CO.

X-ray photoelectron spectroscopy (XPS) was carried out on a PHI QUANTUM 2000 Scanning ESCA Microprobe instrument with an Al Kα radiation source ($h\nu = 1486.6$ eV). The binding energy was calibrated from that of C 1s (284.6 eV).

3. Results and discussion

3.1. Physical properties

Fig. 1 shows the low-angle XRD pattern of mesoporous FeSBA-15 with various Fe contents. The diffraction peaks at 0.88°, 1.44°,

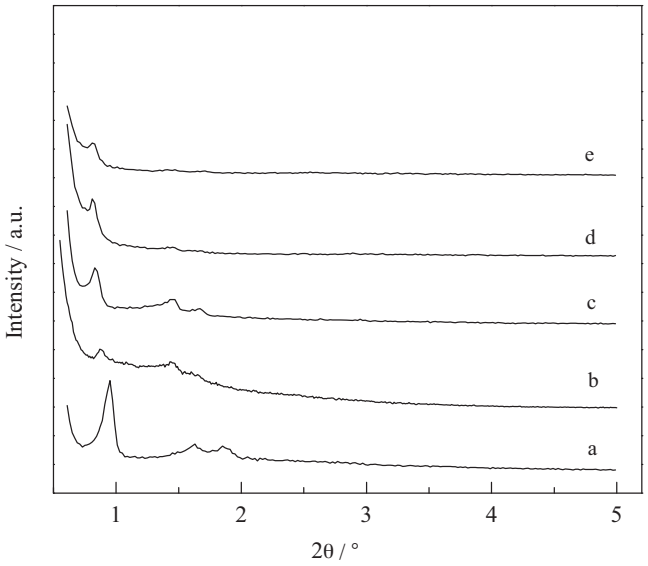

Fig. 1. Low-angle XRD patterns of (a) SBA-15, (b) 0.55% FeSBA-15, (c) 1.07% FeSBA-15, (d) 1.58% FeSBA-15, and (e) 2% Ru/1.07% FeSBA-15.

and 1.64° are respectively assigned to (100), (110), and (200) with *p6mm* symmetry. This result indicates that FeSBA-15 possesses a highly ordered mesoporous structure. The intensities of the diffraction peaks are lower than those of SBA-15 are attributed to the larger radius of ionic Fe^{3+} and bond length of Fe—O than those of Si^{4+} and Si—O, respectively [24]. UV–Vis DRS measurement was used to investigate the structures. Compared with SBA-15, FeSBA-15 exhibits a single and strong adsorption peak at around 254 nm (Fig. 2) because of the dπ–pπ charge transfer between Fe and O in the Fe–O–Si wall [25]. No significant adsorption peak is observed at 320 nm, demonstrating the absence of iron oligomer or ferric oxide species in FeSBA-15 samples [26]. The UV–Vis DRS of as-reduced 2% Ru/1.07% FeSBA-15 catalyst is similar to that of FeSBA-15. The results of XRD, TEM, and UV–Vis DRS for mesoporous FeSBA-15 and as-reduced Ru/FeSBA-15 confirm that the Fe cation is successfully incorporated into the silicate wall of SBA-15.

The actual Fe content in FeSBA-15 and the Ru loading were detected by XRF measurements. Table 1 implies that the actual Ru loadings are slightly lower than the theoretical values.

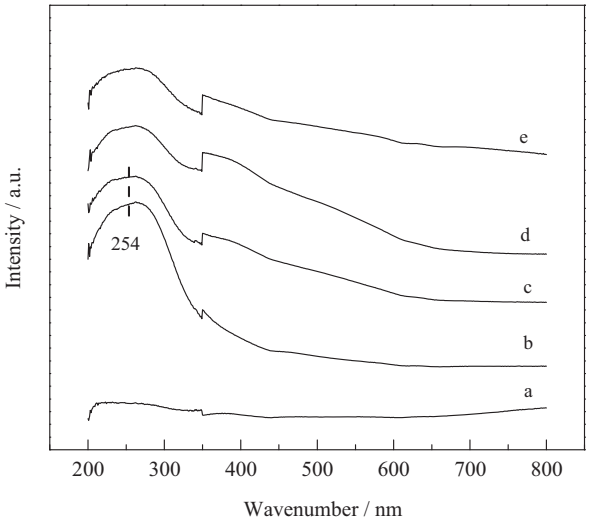

Fig. 2. UV–Vis spectra of (a) SBA-15, (b) 0.55% FeSBA-15, (c) 1.07% FeSBA-15, (d) 1.58% FeSBA-15, and (e) 2% Ru/1.07% FeSBA-15.

Mesoporous FeSBA-15 samples show a lower surface area (325 m^2/g) than SBA-15 (716 m^2/g) owing to the introduction of Fe species. The pore volume of FeSBA-15 samples increase from 0.77 cm^3/g to 1.0 cm^3/g because of the successful addition of the Fe cation into SBA-15. The BET surface area of the Ru/FeSBA-15 catalysts slightly decreases compared with that of the FeSBA-15 support. However, the pore size remains at 11 nm, which is similar to that of the FeSBA-15 support. The results confirm that the Ru species are successfully introduced into FeSBA-15 without collapsing the mesoporous structure.

3.2. XRD and TEM analyses

Figs. S1 and S2 show the XRD patterns of as-reduced 2% Ru/*y*% FeSBA-15 and *x*% Ru/1.07% FeSBA-15 catalysts. No apparent diffraction peaks of Ru species are observed. Furthermore, the mesoporous FeSBA-15 or *x*% Ru/*y*% FeSBA-15 catalysts exhibit no characteristic peaks of the crystalline Fe species. The results from the XRD patterns indicate that Ru and Fe species are highly dispersed on mesoporous FeSBA-15 or SBA-15 supports.

TEM images and particle size distributions are shown in Figs. 3 and S3. The channel structure of 1.07% FeSBA-15 is regular and well-defined (Fig. 3a). For *x*% Ru/1.07% FeSBA-15 catalysts, the average particle size increases from 3.0 nm to 4.0 nm with increasing Ru loading. The mean particle size of 2% Ru/*y*% FeSBA-15 catalysts with different Fe contents remains almost constant at around 3.1 nm (Fig. S3). The results imply that Ru is well-dispersed on the Fe-incorporated mesoporous supports.

The particle structure was characterized by HRTEM (Fig. S4). The representative HRTEM image of the as-reduced 2% Ru/1.07% FeSBA-15 catalyst indicates that the intervals (0.222 and 0.210 nm) between two lattice fringes are slightly smaller than the (100) and (200) lattice spacings of Ru with $p6_3/mmc$ structure, but larger than the (110) and (200) lattice spacings of iron with cubic Im_3m structure. Ru-interacting Fe species reduce to Fe^0 in the form of Ru–Fe alloys. Other Fe species exist as Fe–O–Si in the SBA-15 skeleton based on the UV–Vis DRS characterization (Fig. 2e).

3.3. H_2-TPR

In the case of 1.07% FeSBA-15, the two weak peaks at 675 and 853 K are assigned to the reductions of $Fe^{3+} \rightarrow Fe^{2+}$ and $Fe^{2+} \rightarrow Fe^0$, respectively (Fig. 4). The asymmetric peak in the TPR curve of 2% Ru/SBA-15 reveals the uneven distribution of the nanoparticle size. Given the introduction of Fe into 2% Ru/SBA-15, the reduction temperature of Ru oxide shifts to high temperatures with broadening and symmetric peaks. The results from the H_2-TPR profiles suggest that some interactions between Ru and Fe occur. The 2% Ru–1% Fe/SBA-15-IM catalyst exhibits a highly prominent peak compared with 2% Ru/1.07% FeSBA-15 because of the existence of Ru and Fe species and Ru–Fe bimetallic particles. Fig. S5 shows that one peak at 423 K in the H_2-TPR curve of as-calcined 1% Ru/1.07% FeSBA-15 is caused by the reduction of $Ru^{4+} \rightarrow Ru^0$ with highly dispersion of Ru species. The reduction temperature of Ru oxide increases from 423 to 432 K with increasing Ru amount; this increase is attributed to the increase in the particle size of *x*% Ru/1.07% FeSBA-15. The reduction of Ru oxide in Ru–Fe bimetallic catalysts is different from that of monometallic Ru/SBA-15. The existence of non-noble metals is known to have a negative effect on reduction of noble metal oxides [27].

3.4. XPS analysis

To further characterize the changes in elemental valence on the catalyst surfaces, XPS measurement was performed on the 1.07% FeSBA-15 and 2% Ru/1.07% FeSBA-15 catalysts. Fig. 5 shows the

Table 1
Physical properties of the catalysts.

Catalyst	Ru[a] (wt%)	S_{BET} (m^2/g)	V_{pore} [b] (cm^3/g)	D_{pore} (nm)	Ru particle size[c] (nm)	D_{Ru} [d] (%)
SBA-15	–	715.5	0.77	4.5	–	–
0.55% FeSBA-15	0.55	372.5	1.10	10.8	–	–
1.07% FeSBA-15	1.07	329.1	1.02	10.8	–	–
1.58% FeSBA-15	1.58	325.2	0.98	10.3	–	–
2% Ru/SBA-15	1.98	682.7	0.80	5.0	3.0	28.3
2% Ru–1% Fe/SBA-15-IM	1.95	703.2	0.80	4.9	3.2	25.5
2% Ru/0.55% FeSBA-15	1.95	280.6	0.91	11.1	3.2	27.6
2% Ru/1.07% FeSBA-15	1.98	313.9	1.10	11.9	3.4	25.2
2% Ru/1.58% FeSBA-15	1.93	327.1	1.10	11.6	3.1	27.9
1% Ru/1.07% FeSBA-15	0.96	316.5	1.05	11.2	3.0	26.3
3% Ru/1.07% FeSBA-15	2.94	304.0	1.05	12.0	4.0	24.4

[a] Metal loading was determined by XRF.
[b] Obtained from $P/P_0 = 0.99$.
[c] The particle size was estimated from the TEM image.
[d] Ru dispersion was calculated using the chemisorbed CO.

Fe 2p and Ru 4p XPS data of 1.07% FeSBA-15 and 2% Ru/1.07% FeSBA-15 catalysts before and after reduction. Table S3 shows the deconvolution results. The peak at around 711.1 eV for as-calcined or as-reduced 1.07% FeSBA-15 is attributed to Fe^{3+} ($2p_{3/2}$), which demonstrates the presence of Fe^{3+} species. The Fe oxides on 1.07% FeSBA-15 is nearly not reduced under the corresponding conditions. The similarity of the spectra of as-calcined 2% Ru/1.07% FeSBA-15 and 1.07% FeSBA-15 indicates the existence of Fe^{3+} species. However, the peak at 707 eV is assigned to the metallic Fe [28–31]. This result confirms that partial Fe^{3+} species are reduced upon the addition of Ru. This finding supports the results from UV–Vis DRS and HRTEM that some Fe species interact with Ru reduce to metallic Fe in alloy forms; the rest of Fe species remains tetrahedrally coordinated in the FeSBA-15 framework. The marked binding energy shift from 462.1 to 461.6 eV (Fig. 5c) implies that RuO_2 reduces to metallic Ru under the present conditions.

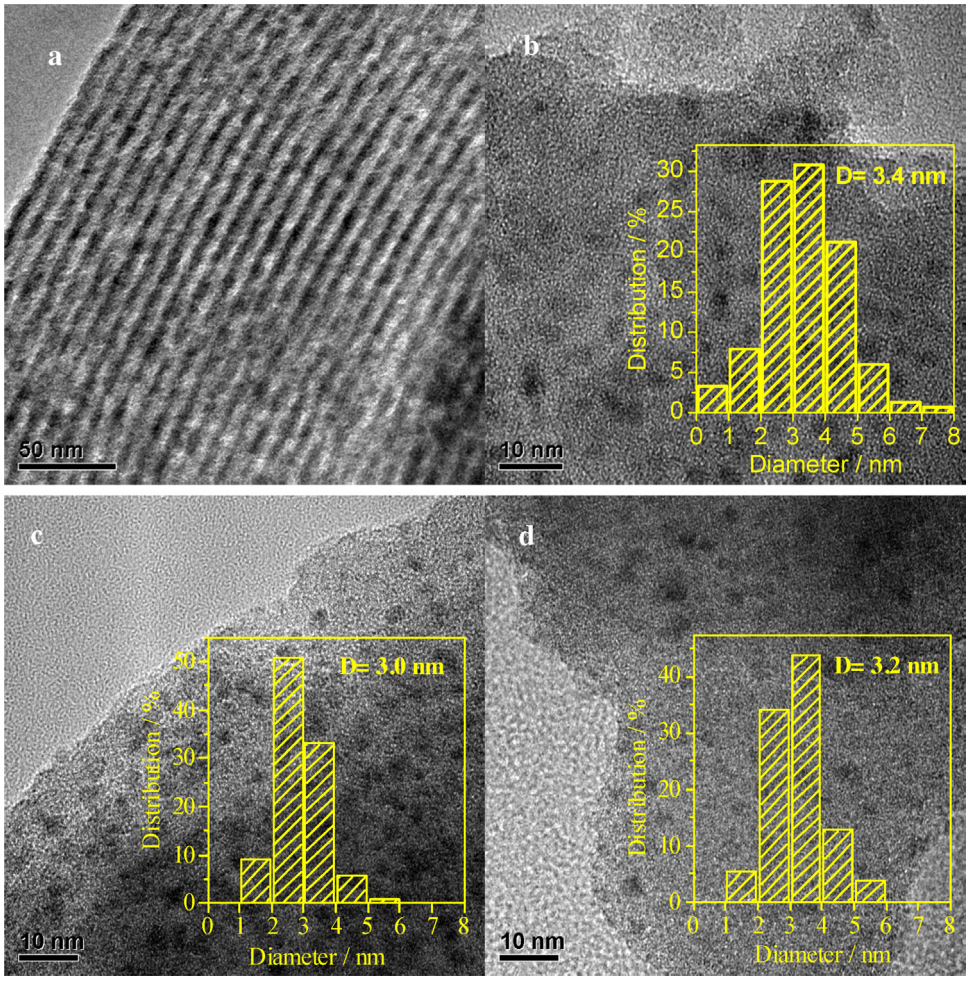

Fig. 3. TEM images and particle size distributions of (a) 1.07% FeSBA-15, (b) 2% Ru/1.07% FeSBA-15, (c) 2% Ru/SBA-15, and (d) 2% Ru–1% Fe/SBA-15-IM.

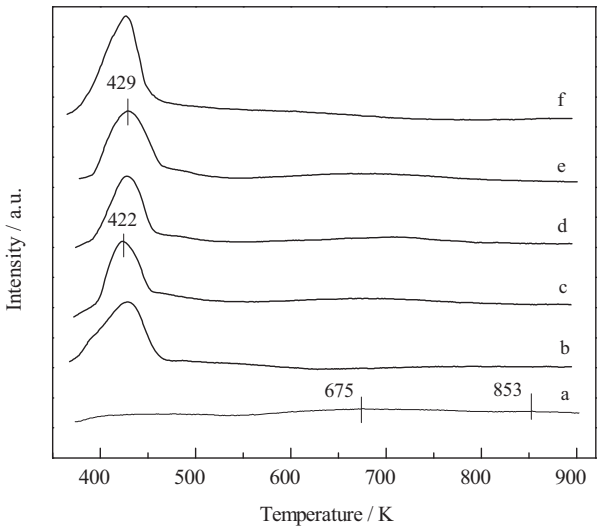

Fig. 4. H_2-TPR profiles of (a) 1.07% FeSBA-15, (b) 2% Ru/SBA-15, (c) 2% Ru/0.55% FeSBA-15, (d) 2% Ru/1.07% FeSBA-15, (e) 2% Ru/1.58% FeSBA-15, and (f) 2% Ru–1% Fe/SBA-15-IM.

3.5. Hydrogenolysis of carboxylic acids

The catalytic performance for the AcOH hydrogenolysis at 523 K was determined to analyze the effect of Fe additives on the catalytic activity and product selectivity over the FeSBA-15-supported Ru catalysts. For the AcOH hydrogenolysis over Ru-based catalysts, the products comprise EtOH, acetaldehyde (AH), ethyl acetate (EtOAc), acetone, and gases (e.g., methane, ethane, and CO_x). As shown in Table 2, the monometallic 2% Ru/SBA-15 catalyst exhibits a poor catalytic activity for AcOH hydrogenolysis with 21.5% AcOH conversion and 84.5% gas selectivity; this result indicates that the catalyst has a higher activity for the cleavage of C—C bonds. The low AcOH conversion over 1.07% FeSBA-15 shows that monometallic FeSBA-15 catalyst possesses nearly no catalytic activity to hydrogenolyze AcOH under the current conditions. However, the Ru–Fe bimetallic catalysts distinctly behave during the AcOH hydrogenolysis. Given the introduction of a small amount of Fe (0.55% content) into 2% Ru/SBA-15, the AcOH conversion reaches 79.9% with 78.2% EtOH selectivity. The 2% Ru/1.07% FeSBA-15 catalyst exhibits the highest catalytic activities of 92.5% AcOH conversion and 85.2% EtOH selectivity when the Fe content increases to 1.07%. Nevertheless, the AcOH conversion and EtOH selectivity reduces if the Fe content in SBA-15 further increases. Hence, the catalytic performance of AcOH hydrogenolysis over Ru-based catalysts possesses a volcano-like tendency with increasing Fe content. The respective AcOH conversion and EtOH selectivity reduce to 73.1% and 74.8% when the catalyst 2% Ru–1% Fe/SBA-15-IM is prepared by using SBA-15 as the support and co-impregnation methods with similar components to 2% Ru/1.07% FeSBA-15; however, the gas selectivity increases to 19.1%.

Subsequently, 1.07% FeSBA-15 was selected as the support to prepare the Ru–Fe bimetallic catalysts with various Ru contents (*x*% Ru/1.07% FeSBA-15); the effects of the Ru contents on the bimetallic catalysts were analyzed. AcOH conversion increases from 50.9% to nearly 100% and the EtOH selectivity decreases with increasing Ru content from 1% to 3%; a high amount of gas-phase products is also obtained.

The turnover frequency (TOF) of several catalysts at 523 K is also incorporated in Table 2. The TOF of Ru–Fe bimetallic catalyst is higher than that of monometallic 2% Ru/SBA-15 and goes through a volcano-like trend as a function of Fe content. The maximum TOF of 468.0 h^{-1} is obtained with the 2% Ru/1.07% FeSBA-15 catalyst.

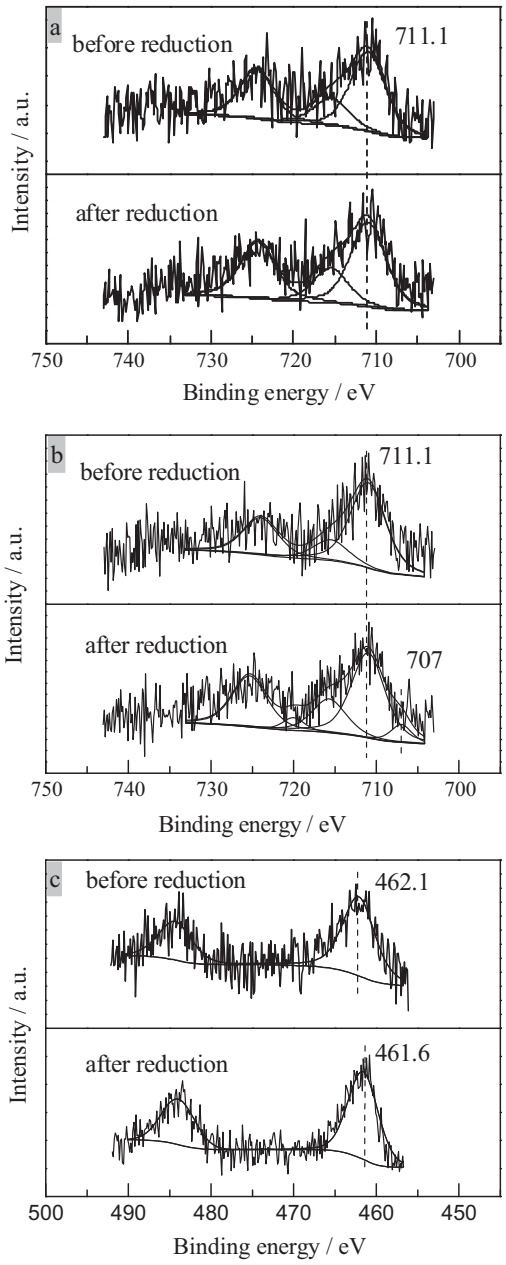

Fig. 5. Fe 2p and Ru 4p XPS of 1.07% FeSBA-15 and 2% Ru/1.07% FeSBA-15 catalysts before and after reduction. (a) Fe 2p spectra of 1.07% FeSBA-15. (b) Fe 2p spectra of 2% Ru/1.07% FeSBA-15 catalyst. (c) Ru 4p spectra of 2% Ru/1.07% FeSBA-15 catalyst.

Further, the TOF of *x*% Ru/1.07% FeSBA-15 catalysts decreases with increasing Ru content (Table S2). This reduction is attributed to the poor dispersion of Ru nanoparticles with increasing Ru content. In brief, the 2% Ru/1.07% FeSBA-15 catalyst exhibits the maximum EtOH yield. The results of the catalytic performances of the FeSBA-15-supported, Ru-based catalysts and other catalysts indicate that the addition of Fe positively affects the AcOH hydrogenolysis to EtOH. We previously demonstrated that some Fe species that were dispersed on the bimetallic catalysts could function as adsorption sites for AcOH [17].

The hydrogenolysis of propionic acid, butyric acid, levulinic acid, and lactic acid were performed to determine the performance of the optimized 2% Ru/1.07% FeSBA-15 catalyst (Table 3). The hydrogenolysis of propionic acid yields a 86.3% conversion and 88.5% propanol selectivity under the conditions to that of AcOH. The butanol selectivity is 87.4% when butyric acid is used as the

Table 2
Catalytic performance for AcOH hydrogenolysis.

Catalyst[a]	Conversion (%)	Selectivity (%)					TOF[c] (h^{-1})
		EtOH	EtOAc	AH	Acetone	Gas[b]	
2% Ru/SBA-15	21.5	5.7	6.3	3.4	0.1	84.5	96.9
2% Ru/0.55% FeSBA-15	79.7	78.2	3.6	0.9	0	17.3	373.9
2% Ru/1.07% FeSBA-15	92.5	85.2	2.6	0.9	0	12.3	468.0
2% Ru/1.58% FeSBA-15	85.6	79.7	0.2	0.5	0	19.6	401.3
2% Ru–1% Fe/SBA-15-IM	73.1	74.8	5.3	0.8	0	19.1	371.1
1.07% FeSBA-15	1.6	24.8	15.6	26.3	17.8	15.4	–
1% Ru/1.07% FeSBA-15	50.9	86.6	3.1	0.6	0	9.7	508.9
3% Ru/1.07% FeSBA-15	100	52.5	0.1	1.2	0.1	46.1	351.9

[a] Reaction conditions: catalyst weight = 0.20 g, T = 523 K, $P(H_2)$ = 3.0 MPa, H_2/AcOH = 80, LHSV = 1.5 h^{-1}.
[b] Mainly contains methane, ethane, and CO_x.
[c] The TOF value was calculated based on Ru dispersion.

Table 3
Hydrogenolysis of several acids using 2% Ru/1.07% FeSBA-15 catalyst.

Substrate	Temperature (K)	Pressure (MPa)	Conversion (%)	Selectivity (%)
Acetic acid[a]	533	3.0	95.7	84.9 (ethanol)
Propionic acid[a]	533	3.0	86.3	88.5 (propanol)
Butyric acid[a]	533	3.0	90.6	87.4 (butanol)
Levulinic acid[a]	523	0.75	87.3	83.3 (GVL)
Levulinic acid[a]	523	3.0	93.2	71.8 (MTHF)
Lactic acid[b]	473	3.0	76.1	64.5(1,2-PDO)

[a] Reaction conditions: catalyst weight = 0.20 g, H_2/substrate = 80, LHSV = 1.5 h^{-1}. The pure substrate and reaction were conducted in a stainless tubular fixed-bed reactor.
[b] Reaction conditions: catalyst weight = 0.10 g. 10 mL 5% lactic acid aqueous solution was poured into a 50 mL steel autoclave.

substrate. Theoretically, the steric effect increases with the growth of carbon chain. Acetic acid can interact with the active site more readily than propionic acid, bringing about the result that its conversion is slightly higher than that of propionic acid. However, in our experiments, the slightly differences of catalytic performances between propionic acid and butyric acid may be mainly attributed to the experimental error. The hydrogenolysis of lactic acid in aqueous solution obtains a 76.1% conversion and 64.5% 1,2-propanediol (1,2-PDO) selectivity; the by-products 1-propanol, 2-propanol, and 1,3-propandiol are obtained because of further hydrogenolysis and isomerization. When 2% Ru/1.07% FeSBA-15 is used to hydrogenolyze levulinic acid, 87.3% of this acid is converted to γ-valerolactone (GVL) with a selectivity of 83.3% under H_2 pressure of 0.75 MPa. GVL is ascribed to the hydrogenolysis of a carbonyl group and the subsequent esterification with a carboxylic group. When the H_2 pressure increases to 3.0 MPa, the conversion of levulinic acid slightly increases to 93.2% with 71.8% selectivity to methyltetrahydrofuran (MTHF), which is a product of the intramolecular cyclization of 2,5-pentandiol. These results indicate that the 2% Ru/1.07% FeSBA-15 catalyst can hydrogenolyze various carboxylic acids to their corresponding alcoholic chemicals.

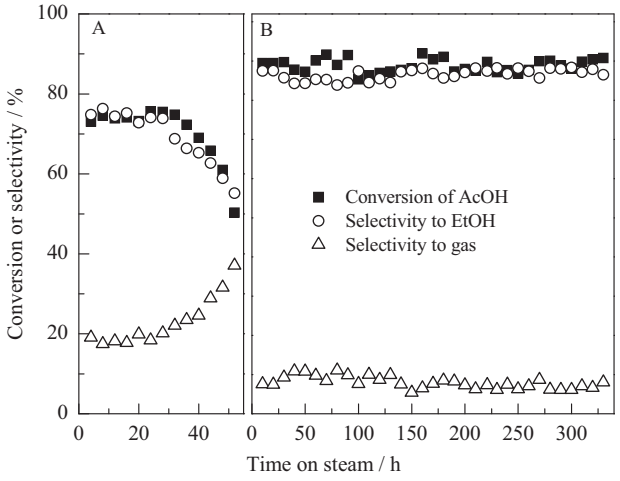

Fig. 6. Catalytic performances of (A) 2% Ru–1% Fe/SBA-15-IM and (B) 2% Ru/1.07% FeSBA-15 at a temperature of 523 K, pressure of 3.0 MPa, LHSV of 1.5 h^{-1}, and H_2/AcOH of 80.

3.6. Catalyst stability

Fig. 6 shows the long-term catalytic performances of 2% Ru/1.07% FeSBA-15 and 2% Ru–1% Fe/SBA-15-IM. The catalyst 2% Ru–1% Fe/SBA-15-IM gradually deactivates after 50 h. The ICP-AES results reveal that some Fe species are leached because of the corrosion of AcOH during the reaction. However, 2% Ru/1.07% FeSBA-15 yields an AcOH conversion of 89% with about 85% EtOH selectivity for over 330 h under the same conditions. After the reaction, negligible aggregation of Ru nanoparticles and leaching of Fe content occur according to the results of XRD (Fig. S6) and ICP-AES, respectively.

The 2% Ru–1% Fe/SBA-15-IM catalyst was prepared by co-impregnation method. Some of the Fe species did not interacted with Ru to form Ru–Fe alloys on the catalyst surfaces. When the acetic acid is introduced, the isolated FeO_x species can be gradually eroded during the reaction process. In the case of 2% Ru/1.07% FeSBA-15, however, small portion of Fe strongly interacts with Ru by forming Ru–Fe alloys, and the rest of Fe oxide species still exist in the form of Fe–O–Si in the FeSBA-15 framework. In other words, the Fe species in 2% Ru/1.07% FeSBA-15 catalyst are much more robust than those in 2% Ru–1% Fe/SBA-15-IM counterpart.

3.7. Structure–performance correlation

The comparison of monometallic Ru/SBA-15 and bimetallic Ru–Fe catalysts for the hydrogenolysis of carboxylic acids reveals that the performance is improved upon the introduction of Fe. Fe oxide species are crucial for the stabilization of Ru–Fe bimetallic nanoparticles and activation of AcOH molecule during the hydrogenolysis [17]. The ordered mesoporous FeSBA-15-supported Ru catalysts efficiently hydrogenolyze short-chain carboxylic acids (e.g., AcOH, propionic acid, butyric acid, levulinic acid, and lactic

acid) to their corresponding alcoholic chemicals. The 2% Ru/1.07% FeSBA-15 catalyst yields the highest catalytic activity and EtOH selectivity. Meanwhile, 2% Ru–1% Fe/SBA-15-IM exhibits low AcOH conversion and EtOH selectivity, but gives high selectivity to gas-phase by-products. The *x*% Ru/1.07% FeSBA-15 catalysts with high Ru content display high AcOH conversion and selectivities to gas-phase by-products.

Combining with the results of spectroscopic study, we consider that the Fe species in the framework of SBA-15 may have two functions. Small portion of Fe strongly interacts with Ru by forming Ru–Fe alloys, which may adjust the ability of activating hydrogen molecule, resulting in a tremendous enhancement in selectivity to alcoholic product due to the C—O bond cleavage. The rest of Fe oxide species are still highly dispersed in the frameworks of SBA-15, providing the adsorption sites for acidic substrates and thus promoting the reaction. When calculating the TOF values of the catalysts with different Fe contents, we find that only the catalyst with a proper Ru/Fe ratio likely 2% Ru/1.07% FeSBA-15 supremely benefits from the synergistic effect of the Ru–Fe alloy and Fe oxides either at higher or lower reaction temperatures (Tables 2 and S1).

However, no significant peaks but a very weak and broad band between 450 and 600 nm due to the addition of Ru into FeSBA-15 can be observed in the UV–Vis (Fig. 2). The reason may be due to the fact that the Ru–Fe alloys form just in the interface instead of the whole nanoparticle. That is to say, it cannot obtain substantial evidences for the Ru–Fe interactions by UV–Vis measurement. Nevertheless, the XPS data in Table S3 show that the Fe species in FeSBA-15 are barely reduced under the present reduction conditions, but in 2% Ru/1.07% FeSBA-15 catalyst, 11.5% of Fe species are reduced to metallic Fe species. The XPS results provide a strong evidence for the Ru–Fe interactions.

The correlation between the performance and structure of the catalysts suggests that the improvement is caused by the coherent interactions between Fe and Ru species and the high dispersion of Fe oxides in the SBA-15 framework. The results are attributed to the complicated structure of 2% Ru–1% Fe/SBA-15-IM with Ru–Fe bimetallic particles, isolated Ru species, and Fe-oxides. As for the *x*% Ru/1.07% FeSBA-15 catalysts with higher Ru loadings, the limited Fe species come out from the FeSBA-15 framework results in the Ru–Fe alloys with excess amount of Ru. As a result, AcOH is excessively hydrogenolyzed and high amount of CH_4 is obtained from the breakage of C—C bonds. Therefore, the appropriate composition of Ru–Fe active sites and the high dispersion of Fe promoters cause the high EtOH yield for the 2% Ru/1.07% FeSBA-15 catalyst.

4. Conclusion

In this study, FeSBA-15 mesoporous materials with different Fe contents are synthesized and used as supports to prepare Ru–Fe bimetallic catalysts. Given the introduction of Ru, a small portion of Fe reduces and interacts with Ru in the form of Ru–Fe alloys; the other Fe species remain in the framework of SBA-15 during the reduction pretreatment. The results of characterization and catalytic performance confirm that the Fe and Ru contents exhibit important functions in the hydrogenolysis of carboxylic acids to produce the corresponding alcoholic chemicals. The optimal EtOH yield (AcOH conversion, 92.5%; EtOH selectivity, 85.2%) is obtained for the 2% Ru/1.07% FeSBA-15 catalyst, which is highly stable because its high activity during AcOH hydrogenolysis is maintained for over 330 h.

Acknowledgements

We acknowledge the financial supports from the MOST of China (2011CBA00508), the NSFC (21173175, 21303141, 21403178 and 21473145), and the Research Fund for the Doctoral Program of Higher Education (20110121130002).

Appendix A. Supplementary data

Supplementary data associated with this article can be found, in the online version, at http://dx.doi.org/10.1016/j.cattod.2014.10.044.

References

[1] Y. Lin, S. Tanaka, Appl. Microbiol. Biotechnol. 69 (2006) 627–642.
[2] M.T. Holtzapple, C.B. Granda, Appl. Biochem. Biotechnol. 156 (2009) 525–536.
[3] H.N. Chang, N.J. Kim, J.W. Kang, C.M. Jeong, Biotechnol. Bioprocess Eng. 15 (2010) 1–10.
[4] T. Eggeman, D. Verser, E. Weber, An Indirect Route for Ethanol Production, US Department of Energy, Zeachem Inc., 2005, DE-FG-03GO13010.
[5] Y. Nakagawa, K. Tomishige, Catal. Surv. Asia 15 (2011) 111–116.
[6] L.M. He, H.Y. Cheng, G.F. Liang, Y.C. Yu, F.Y. Zhao, Appl. Catal. A: Gen. 452 (2013) 88–93.
[7] L.H. Tan Tai, V. Nardello-Rataj, in: U. Zoller (Ed.), Handbook of Detergents Part E: Applications, CRC Press, Taylor and Francis Group, Boca Raton, 2009, p. 110.
[8] J.L. Hargrove, P. Greenspan, D.K. Hartle, Exp. Biol. Med. 229 (2004) 215–226.
[9] Y. Ni, P.L. Hagedoorn, J.H. Xu, I.W.C.E. Arends, F. Hollmann, Chem. Commun. 48 (2012) 12056–12058.
[10] W. Rachmady, M.A. Vannice, J. Catal. 192 (2000) 322–334.
[11] W. Rachmady, M.A. Vannice, J. Catal. 207 (2002) 317–330.
[12] G. Onyestyák, S. Harnos, S. Klébert, M. Štolcová, A. Kaszonyi, D. Kalló, Appl. Catal. A: Gen. 464 (2013) 313–321.
[13] J. ten Dam, U. Hanefeld, ChemSusChem 4 (2011) 1017–1034.
[14] C. Luo, S. Wang, H.C. Liu, Angew. Chem. Int. Ed. 46 (2007) 7636–7639.
[15] H.J. Wan, R.V. Chaudhari, B. Subramaniam, Energy Fuels 27 (2012) 487–493.
[16] S.B. Zhang, X.P. Duan, L.M. Ye, H.Q. Lin, Z.X. Xie, Y.Z. Yuan, Catal. Today 215 (2013) 260–266.
[17] W.J. Li, L.M. Ye, P. Long, J. Chen, H. Ariga, K. Asakura, Y.Z. Yuan, RSC Adv. 4 (2014) 29072–29082.
[18] H. Olcay, Y. Xu, G.W. Huber, Green Chem. 16 (2014) 911–924.
[19] T. Jiang, Y.X. Zhou, S.G. Liang, H.Z. Liu, B.X. Han, Green Chem. 11 (2009) 1000–1006.
[20] T. Miyake, T. Makino, S.-i. Taniguchi, H. Watanuki, T. Niki, S. Shimizu, Y. Kojima, M. Sano, Appl. Catal. A: Gen. 364 (2009) 108–112.
[21] M. Toba, S.-i. Tanaka, S.-i. Niwa, F. Mizukami, Z. Koppány, L. Guczi, K.-Y. Cheah, T.-S. Tang, Appl. Catal. A: Gen. 189 (1999) 243–250.
[22] Y. Li, Z.C. Feng, Y.X. Lian, K.Q. Sun, L. Zhang, G.Q. Jia, Q.H. Yang, C. Li, Microporous Mesoporous Mater. 84 (2005) 41–49.
[23] D. Zhao, Q. Huo, J. Feng, B.F. Chmelka, G.D. Stucky, J. Am. Chem. Soc. 120 (1998) 6024–6036.
[24] H. Huang, Y. Ji, Z. Qiao, C. Zhao, J. He, H. Zhang, J. Anal. Method Chem. 2010 (2010) 1–7.
[25] Y.C. Du, S. Liu, Y.Y. Ji, Y.L. Zhang, F.J. Liu, Q. Gao, F.S. Xiao, Catal. Today 131 (2008) 70–75.
[26] A. Tuel, I. Arcon, J.M. Millet, J. Chem. Soc. Faraday Trans. 94 (1998) 3501–3510.
[27] R. Burch, M.J. Hayes, J. Catal. 165 (1997) 249–261.
[28] C.R. Brundle, T.J. Chuang, K. Wandelt, Surf. Sci. 68 (1977) 459–468.
[29] N. McIntyre, D. Zetaruk, Anal. Chem. 49 (1977) 1521–1529.
[30] B.D. Li, J. Wang, Y.Z. Yuan, H. Ariga, S. Takakusagi, K. Asakura, ACS Catal. 1 (2011) 1521–1528.
[31] V. Schünemann, H. Trevino, W.M.H. Sachtler, K. Fogash, J.A. Dumesic, J. Phys. Chem. 99 (1995) 1317–1321.